INTERNATIONAL JOURNAL OF
NUMERICAL ANALYSIS AND MODELING
Volume 12, Number 2, Pages 268–285

PHASE FIELD SIMULATION OF DROP FORMATION IN A COFLOWING FLUID

JIEWEI LIU* AND XIAO-PING WANG

Abstract. We numerically investigate the dynamics of drop formation when a Newtonian fluid is injected through a tube into another immiscible, co-flowing Newtonian fluid with different density and viscosity using the phase field method. The two phase system is modeled by a coupled three dimensional Cahn-Hilliard and Navier-Stokes equation in cylindrical coordinates. And the contribution from the chemical potential has been taken into account in the classical Navier-Stokes equation. The numerical method involves a convex splitting scheme for the Cahn-Hilliard equation and a projection type scheme for the momentum equation. Our study of the dynamics of the drop formation is motivated by the experimental work by Utada *et al* [*Phys. Rev. Lett.* **99**(2007), 094502] on dripping and jetting transition. The simulation results demonstrate that the process of drop formation can be reasonably predicated by the phase field model we used. Our simulations also identify two classes of dripping to jetting transition, one controlled by the Capillary number of the outer fluid and another one controlled by the Weber number of the inner fluid. The results match well with the experimental results in Utada *et al* [A. S. Utada, A. Fernandez-Nieves, H. A. Stone, and D. A. Weitz, *Phys. Rev. Lett.* **99**(2007), 094502] and Zhang [*Chem. Eng. Sci.* **54**(1999), 1759-1774]. We also study how the dynamics of the drop formation depends on the various physical parameters of the system. Similar behaviors with existing results are obtained for most parameters, yet different behavior is observed for density ratio λ_ρ and viscosity ratio λ_η.

Key words. Two phase flows, coflowing, phase field method, dripping, jetting.

1. Introduction

Dispersion of one fluid into another fluid through a vertical tube is of great importance in scientific research because of its widespread applications in the industrial production, like copolymers, cosmetics, capsules and pharmaceutics (Hua et al. [16]). The potential use of the dispersion technology is always limited by its ability to precisely control the size distribution of the droplets (Carlson et al.[5]). Over the last decade, many experiments have been carried out (A. M. Gañán-Calvo [9], Umbanhowar et al. [31], Gañán-Calvo et al. [10], Cramer et al. [6], Garstecki et al. [11], Utada et al. [30]), aiming at developing technologies to produce mono-disperse droplets with controllable size. It is found that a coflowing outer fluid or flow-focusing technique could produce smaller drops and give rise to mono-dispersion (Chuang et al. [7], Gañán-Calvo et al. [10], Utada et al. [30]).

Numerical simulation serves as a good complementary to the experimental investigation and theoretical analysis. Numerical methods for simulating multi-phase problems can be divided into two classes: sharp interface method and diffuse interface method. The advantage of the diffuse interface method is its ability to handle

Received by the editors March 9, 2014.
2000 *Mathematics Subject Classification.* 65M12, 65M70, 65P99.
*Corresponding author.
This publication was based on work supported in part by Award No SA-C0040/UK-C0016, made by King Abdullah University of Science and Technology (KAUST), Hong Kong RGC-GRF grants 603107, 604209 and 605311. This work forms part of the first author's PhD thesis under the supervision of the second author. The first author thanks the HKUST for providing Postgraduate Studentship.

the topological change of the interface which is important in the current application to the drop formation and dynamics.

Many numerical studies have been carried out for the coflowing fluid-fluid system using the sharp interface methods. Oguz and Prosperetti [19] studied the dynamics of gas bubble growth and detachment in a liquid for ir-rotational flow using a boundary integral method. As a complementary to the research by Oguz and Prosperetti [19] that focused mainly on inertial effect, Wong et al. [32] studied the motion of a pinned gas bubble expanding or contracting from a submerged capillary tip for flows with low Reynolds number using the boundary integral method. Zhang and Stone [36] studied drop formation in a quiescent and coflowing fluid by solving the governing Stokes equation using the boundary integral method, with the main focus on the assessment of the influence of three dimensionless number on drop evolution and breakup. In a series papers, Richards et al. [22, 23, 24] developed a robust and stable numerical method which combined the volume-of-fluid (VOF) method [15] and the continuous-surface-force (CSF) method [2] to simulate liquid-liquid systems. Using the same numerical method as Richards et al. [22, 23, 24], Zhang [34] investigated the drop formation dynamics in the dripping region and found good agreement with his experiment. More recently, Suryo and Basaran [27] studied the tip streaming forming from a tube in a coflowing outer fluid under creeping flow conditions. They solved the Stokes equations using the Galerkin finite element method for spatial discretization and adaptive finite difference method for time integration.

Diffuse interface method has also been used to simulate the drop formation and dynamics. Zhou et al. [35] investigated drop formation in the quiescent air and flows in a flow-focus device. The dynamics of drop formation can be classified into two regimes. One is dripping, and the other is jetting. Previous research on coflowing fluid mainly focus on the dynamics of liquid drop or gas bubble. The transition from dripping to jetting has not been studied numerically, to the author's knowledge. In this paper, we give a systematic numerically studies of drop formation dynamics in a three dimensional coflowing fluid-fluid system in cylindrical coordinates. The motion of the interface is modeled by a diffuse interface model consisting of the Cahn-Hilliard Navier-Stokes equations. The numerical method involves a convex splitting scheme for the Cahn-Hilliard equation and a projection type scheme for the Navier-Stokes equation. We study how the dynamics of the drop formation depends on the various physical parameters of the system. In particular, we are interested in the dripping to jetting transition behavior.

The rest of this paper is organized as follows: In section 2, we describe the mathematical formulation of the problem, including governing equations, boundary and initial conditions, in both dimensional and dimensionless form. In section 3, we present the numerical method for solving the Cahn-Hilliard Navier-Stokes equations with different density and viscosity ratio. Section 4 shows our numerical results and the comparison with the experiments. Two different classes of dripping-to-jetting transition observed in the experimental paper [29] are identified. Section 5 is the conclusion.

2. Problem formulation

In our problem, an incompressible Newtonian fluid with density ρ_i and viscosity η_i is injected through a vertical capillary tube of radius R_i into a coflowing, immiscible, incompressible Newtonian fluid with density ρ_o and viscosity η_o, the outer fluid is contained in a coaxial cylindrical tube of radius R_o. The dispersed phase and the continuous phase flow at constant flow rates of Q_i and Q_o respectively. A schematic diagram is shown in Figure 1. It is convenient to adopt the cylindrical coordinate system $\{r, z, \theta\}$ with its origin at the intersection of the centerline c_l and the inflow boundary $z = 0$, where $\{r, z, \theta\}$ represent the radial coordinate, axial coordinate and azimuthal angle respectively. We assume radial symmetry, therefore all variables are independent of the azimuthal angle θ.

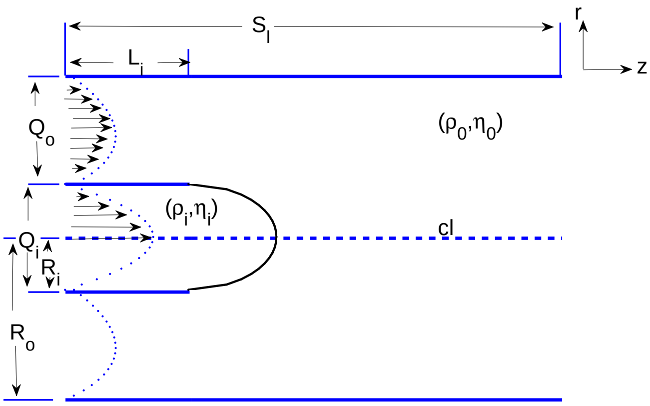

FIGURE 1. Schematic diagram of drop formation in another coflowing fluid.

The phase field model of the two phase system consists of Cahn-Hilliard equation

$$\frac{\partial \phi}{\partial t} + \mathbf{v} \cdot \bigtriangledown \phi = M \bigtriangleup \mu, \tag{1}$$

where

$$\mu = -K \bigtriangleup \phi - r\phi + u\phi^3; \tag{2}$$

and Navier-Stokes equation with the contribution from the chemical potential

$$\rho[\frac{\partial \mathbf{v}}{\partial t} + (\mathbf{v} \cdot \bigtriangledown)\mathbf{v}] = -\bigtriangledown p + \bigtriangledown \cdot [\eta D(\mathbf{v})] + \mu \bigtriangledown \phi + \rho \mathbf{g}; \tag{3}$$

with incompressibility condition

$$\bigtriangledown \cdot \mathbf{v} = 0; \tag{4}$$

Density and viscosity are assumed as an interpolation function of ϕ,

$$\rho = \rho_i \frac{1-\phi}{2} + \rho_o \frac{1+\phi}{2}, \quad \eta = \eta_i \frac{1-\phi}{2} + \eta_o \frac{1+\phi}{2}. \tag{5}$$

In equations (1)-(5), μ is the chemical potential, $\mathbf{v} = \{u_z, u_r\}$ is the fluid velocity where u_z and u_r represent the axial and radial components respectively, p is the pressure, $\mathbf{g} = (g, 0)$ with g being the gravitational acceleration constant, $D(\mathbf{v}) = \bigtriangledown \mathbf{v} + \bigtriangledown \mathbf{v}^T$ is the strain rate. Parameters K, r, u in equation (2) originated from the free energy of the system $F[\phi] = \int d\mathbf{r} = [\frac{1}{2}K(\nabla\phi)^2 - \frac{1}{2}r\phi^2 + \frac{1}{4}u\phi^4]$ [20], and are relate to the interface thickness $\xi = \sqrt{K/r}$, the interfacial tension $\gamma = 2\sqrt{2}r^2\xi/3u$, and the two homogeneous equilibrium phases $\phi_{\pm} = \pm\sqrt{r/u}$ ($= \pm 1$ in our problem), M is the phenomenological mobility coefficient[21].

The system (1)-(5) is solved subjected to the following boundary conditions. The three phase contact line, where the interface of the inner and outer fluids meets the solid surface, is assumed to be pinned to the sharp edge of the tube at all time, as in the paper of Zhang [34]. No-slip and no-penetration conditions are imposed along the solid walls of the inner and outer tubes,

$$\mathbf{v} = 0, \quad \text{at } \{r = R_i, 0 \le z \le L_i\} \text{ or at } r = R_o. \tag{6}$$

$$\frac{\partial \mu}{\partial r} = 0, \quad \frac{\partial \phi}{\partial r} = 0, \quad \text{at } \{r = R_i, 0 \le z \le L_i\} \text{ or at } r = R_o. \tag{7}$$

Well upstream of the tube exit, the inflow condition at $z = 0$ for the inner tube is

$$u_r(0, r, t) = 0, \quad u_z(0, r, t) = 2\frac{Q_i}{\pi R_i^2}[1 - (\frac{r}{R_i})^2], \quad \text{for } 0 \le r \le R_i. \tag{8}$$

And that for the outer tube is the fully developed velocity profile, according to Bird et al. [3],

$$u_r(0, r, t) = 0, \quad u_z(0, r, t) = 2\frac{Q_o}{\pi R_o^2}[\frac{1 - (\frac{r}{R_o})^2 + \frac{1-(R_i/R_o)^2}{\ln(R_o/R_i)}\ln(\frac{r}{R_o})}{1 - (\frac{R_i}{R_o})^4 - \frac{(1-(R_i/R_o)^2)^2}{\ln(R_o/R_i)}}], \tag{9}$$

$$\text{for } R_i \le r \le R_o.$$

The velocity profiles (8)-(9) are also adopted by Suryo and Basaran [27] to study tip streaming under creeping flow conditions. It's easy to check that $\int_0^{R_i} u_z dr = Q_i$ and $\int_{R_i}^{R_o} u_z dr = Q_o$. Inflow boundary conditions for ϕ and μ are

$$\phi(0, r, t) = \begin{cases} -1, \text{ if } 0 \le r \le R_i \\ 1, \text{ if } R_i < r \le R_o \end{cases}, \tag{10}$$

$$\mu(0, r, t) = 0, \quad 0 \le r \le R_o. \tag{11}$$

Along the central line c_l, we use symmetric boundary conditions, *i.e.*,

$$\frac{\partial u_z}{\partial r} = 0, \quad u_r = 0, \quad \frac{\partial \phi}{\partial r} = 0, \quad \frac{\partial \mu}{\partial r} = 0, \quad \text{at } r = 0. \tag{12}$$

Suppose the length of outer tube is long enough such that the outflow condition will not affect the drop formation process significantly, and at the outlet boundary $z = S_l$, we can assume

$$\frac{\partial u_z}{\partial z} = 0, \quad u_r = 0, \quad \frac{\partial \phi}{\partial z} = 0, \quad \frac{\partial \mu}{\partial z} = 0. \tag{13}$$

Initially, both the inner and outer fluids are quiescent, so

$$\mathbf{v}(z, r, 0) = 0, \tag{14}$$

on the whole region. The inner fluid only occupies the inner tube, thus

$$\phi(z, r, 0) = \begin{cases} -1, \text{ if } 0 \le r \le R_i \text{ and } 0 \le z \le L_i \\ 1, \text{ otherwise} \end{cases}. \tag{15}$$

We now introduce the following characteristic scales,

$$l_c = R_i,\ v_c = \tfrac{Q_i}{\pi R_i^2},\ \rho_c = \rho_i,\ \eta_c = \eta_i,\ \phi_c = \sqrt{r/u},$$

then the dimensionless counterpart of the system (1)-(5) are the followings, where we have used the same notations for the dimensionless variables

$$\frac{\partial \phi}{\partial t} + \mathbf{v} \cdot \bigtriangledown \phi = \mathcal{L}_d \bigtriangleup \mu, \tag{16}$$

where

$$\mu = -\epsilon\triangle\phi - \phi/\epsilon + \phi^3/\epsilon, \tag{17}$$

$$\mathcal{R}e\rho[\frac{\partial \mathbf{v}}{\partial t} + (\mathbf{v}\cdot\bigtriangledown)\mathbf{v}] = -\bigtriangledown p + \bigtriangledown\cdot[\eta D(\mathbf{v})] + \mathcal{B}\mu\bigtriangledown\phi + \frac{\mathcal{B}o}{\mathcal{C}a}(\rho-1)\mathbf{j}_z, \tag{18}$$

$$\bigtriangledown\cdot\mathbf{v} = 0, \tag{19}$$

$$\rho = \frac{1-\phi}{2} + \lambda_\rho\frac{1+\phi}{2}, \quad \eta = \frac{1-\phi}{2} + \lambda_\eta\frac{1+\phi}{2}, \tag{20}$$

with the boundary conditions

$$\mathbf{v} = 0, \quad \text{at } \{r = 1, 0 \le z \le L_i\} \text{ or at } r = a. \tag{21}$$

$$\frac{\partial \mu}{\partial r} = 0, \quad \frac{\partial \phi}{\partial r} = 0, \quad \text{at } \{r = 1, 0 \le z \le L_i\} \text{ or at } r = a. \tag{22}$$

The inflow boundary conditions (8)-(11) change to

$$u_r(0,r,t) = 0, \quad u_z(0,r,t) = 2[1-r^2], \quad \text{for } 0 \le r \le 1. \tag{23}$$

(24)

$$u_r(0,r,t) = 0, \quad u_z(0,r,t) = 2\frac{Q_r}{a^2}[\frac{1-(\frac{r}{a})^2 + \frac{1-(1/a)^2}{\ln(a)}\ln(\frac{r}{a})}{1-(\frac{1}{a})^4 - \frac{(1-(1/a)^2)^2}{\ln(a)}}], \quad \text{for } 1 \le r \le a.$$

$$\phi(0,r,t) = \begin{cases} -1, & \text{if } 0 \le r \le 1 \\ 1, & \text{if } 1 < r \le a \end{cases} \tag{25}$$

$$\mu(0,r,t) = 0, \quad 0 \le r \le a. \tag{26}$$

Dimensionless forms of conditions (12)-(14) is the same as their dimensional forms,

$$\frac{\partial u_z}{\partial r} = 0, \quad u_r = 0, \quad \frac{\partial \phi}{\partial r} = 0, \quad \frac{\partial \mu}{\partial r} = 0, \quad \text{at } r = 0. \tag{27}$$

$$\frac{\partial u_z}{\partial z} = 0, \quad u_r = 0, \quad \frac{\partial \phi}{\partial z} = 0, \quad \frac{\partial \mu}{\partial z} = 0, \quad \text{at } z = S_l. \tag{28}$$

$$\mathbf{v}(z,r,0) = 0. \tag{29}$$

And initial condition for ϕ (15) now becomes

$$\phi(z,r,0) = \begin{cases} -1, & \text{if } 0 \le r \le 1 \text{ and } 0 \le z \le L_i \\ 1, & \text{otherwise.} \end{cases} \tag{30}$$

The dimensionless parameters introduced in equation (16)-(30) are Reynolds number $\mathcal{R}e \equiv \frac{\rho_c v_c l_c}{\eta_c} = \frac{\rho_i Q_i}{\eta_i \pi R_i}$, which measures the relative importance of inertial force to viscous force; Capillary number $\mathcal{C}a \equiv \frac{\eta_c v_c}{\gamma} = \frac{\eta_i Q_i}{\gamma\pi R_i^2}$, which measures the relative importance of the viscous force to surface tension force; Bond number $\mathcal{B}o \equiv \frac{\rho_c l_c^2 g}{\gamma} = \frac{\rho_i R_i^2 g}{\gamma}$, which measures the relative importance of the gravitational force to surface tension force; diffusion coefficient $\mathcal{L}_d \equiv \frac{3M\gamma}{2\sqrt{2}v_c {l_c}^2} = \epsilon^2\frac{3M\gamma}{2\sqrt{2}v_c\xi^2} = \frac{3M\gamma\pi}{2\sqrt{2}Q_i}$, where $\frac{3M\gamma}{2\sqrt{2}v_c\xi^2}$ is the ratio of a diffusion length $\frac{Mr}{v_c}$ to the interface thickness ξ, noticing that $\gamma = \frac{2\sqrt{2}r^2\xi}{3u}$ [20]; $\mathcal{B} = \frac{3\gamma}{2\sqrt{2}\eta_c v_c} = \frac{3\gamma\pi R_i^2}{2\sqrt{2}\eta_i Q_i}$, which is inversely proportional to the Capillary number; Cahn number $\epsilon = \frac{\xi}{l_c} = \frac{\xi}{R_i}$, which is the ratio between interface thickness ξ and length scale l_c; $\lambda_\rho = \frac{\rho_o}{\rho_i}$, $\lambda_\eta = \frac{\eta_o}{\eta_i}$, which are the density ratio and viscosity ratio respectively; $Q_r = \frac{Q_o}{Q_i}$, which is the ratio of the flow rate of the outer fluid to that of the inner fluid, and $a = \frac{R_o}{R_i}$, which is the ratio of the radius of the outer tube to that of the inner tube.

3. Numerical methods

One needs to overcome several difficulties when designing algorithm for the system (16)-(30). As pointed out in previous work [28, 26], one difficulty comes from the coupling of the velocity and pressure through the incompressibility constraint; another difficulty comes along with the nonequal density and viscosity of the two fluids; the third difficulty, comes from the 4th order derivatives, nonlinearity [14] and the stiffness of the Cahn-Hilliard equation associated with the interfacial width ϵ. The first difficulty is usually overcome by decoupling the computation of the pressure from the velocity using projection type scheme that was first introduced by Chorin [4]. A detailed review of the projection method is given by Guermond et al. [12]. Most of the current projection methods are limited to problems with constant density and viscosity [26]. Guermond and Salgado [13] proposed a new fractional time-stepping technique to solve incompressible flows with variable density, which we will employ in this paper. As for the Cahn-Hilliard equation, a lot of works have been carried out to develop stable, energy decaying numerical schemes. The stiffness of the phase equation could be eliminated through two methods [28]: one method is to add a stabilizing term in the phase equation, as what has been done in by Yang et al. [33]; the other method is to use the convex splitting approach proposed by Eyre [8]. The second method has been adopted by Gao and Wang [14] to study the moving contact line problem. In the following, we are going to apply the same method of Gao and Wang [14, 37] to solve the system (16)-(30).

The computational domain is

$$\Omega = \{(z, r) \mid 0 \leq z \leq S_l, 0 \leq r \leq a\}, \tag{31}$$

where $r = 0$ corresponds to the z-axis (the centerline) and $r = a$ corresponds to the solid wall of the outer tube, $z = 0$ is the place where the inflow boundary condition is imposed. Divide Ω into $nz \times nr$ smaller cells, with nz, nr being the number of cells in z and r direction. Cell center, right boundary and top boundary are represented by (i, j), $(i + 1/2, j)$, and $(i, j + 1/2)$ respectively. To make it easier for computation, we assume that the solid wall of the inner tube and its exit are in line with the cell boundaries. The radial velocity $u_{r\,i,j+\frac{1}{2}}$ and axial velocity $u_{z\,i+\frac{1}{2},j}$ are defined at the low and left boundary of each cell respectively, whereas the phase filed $\phi_{i,j}$, pressure $p_{i,j}$, chemical potential $\mu_{i,j}$ are located at the center.

Given an initial condition, $\{\phi^0, p^0, v^0, \psi^0\}$, the time stepping algorithm are the following:

- Step 1. Update ϕ^n, μ^n according to

$$\begin{cases} \frac{\phi^{n+1}-\phi^n}{\triangle t} + \mathbf{v}^n \cdot \phi^{n+1} = \mathcal{L}_d \triangle \mu^{n+1} \\ \mu^{n+1} = -\epsilon \triangle \phi^{n+1} + (s\phi^{n+1} - (1+s)\phi^n + (\phi^n)^3)/\epsilon \end{cases} \tag{32}$$

The boundary conditions at the solid walls of the inner and outer tubes, the lower and right boundaries of Ω are the homogeneous Numann B.C. for both ϕ and μ,

$$\frac{\partial \phi^{n+1}}{\partial n} = 0, \quad \frac{\partial \mu^{n+1}}{\partial n} = 0. \tag{33}$$

At the left boundary,

$$\phi^{n+1}(0,r,t) = \begin{cases} -1, \text{ if } 0 \le r \le 1 \\ 1, \text{ otherwise} \end{cases}, \quad \mu^{n+1}(0,r,t) = 0. \tag{34}$$

- Step2. Update ρ^n and η^n according to equation (20).
- Step3. Solve the Navier-Stokes equation using pressure stabilization scheme,

$$\begin{aligned} &\mathcal{R}e[\frac{\frac{1}{2}(\rho^{n+1}+\rho^n)\mathbf{v}^{n+1} - \rho^n\mathbf{v}^n}{\triangle t} + \rho^{n+1}(\mathbf{v}^n \cdot \bigtriangledown)\mathbf{v}^{n+1} + \frac{1}{2}(\bigtriangledown \cdot (\rho^{n+1}\mathbf{v}^n))\mathbf{v}^{n+1}] \\ = \; &\nabla \cdot [\eta^{n+1} D(\mathbf{v}^{n+1})] - \nabla(p^n + \psi^n) + \mathcal{B}\mu^{n+1}\nabla\phi^{n+1} + \frac{\mathcal{B}o}{\mathcal{C}a}(\rho^{n+1} - 1)\mathbf{j}_z. \end{aligned} \tag{35}$$

Boundary conditions for the velocity $\mathbf{v}$ are the inflow boundary conditions (23)-(24) at the left, no-slip boundary condition (21) at the solid walls of the inner and outer tubes, symmetric boundary condition, *i.e.*, the first two formulas of (27) at the centerline, and outflow boundary condition, *i.e.*, the first two formulas of (28) at the right.

- Step4. Update ψ in equation (35) using

$$\triangle\psi^{n+1} = \frac{\chi \cdot \mathcal{R}e}{\triangle t}\nabla \cdot \mathbf{v}^{n+1}, \tag{36}$$

where $\chi \equiv \min_\Omega \rho$. Boundary conditions for ψ at the inflow boundary, the centerline and the solid walls of the inner and outer tubes are

$$\frac{\partial\psi^{n+1}}{\partial n} = 0, \tag{37}$$

and at the right boundary, we use

$$\psi^{n+1} = 0, \tag{38}$$

for simplicity.

- Step5. Update pressure according to

$$p^{n+1} = p^n + \psi^{n+1}. \tag{39}$$

In our problem, we can simply set the initial condition $p^0 = 0$ and $\psi^0 = 0$ because the fluids are quiescent.

Remark 3.1. We discretize the operator $\triangle$ in cylindrical coordinate by the standard finite difference method.

Remark 3.2. Velocity components are defined at the cell boundaries, their values at the cell center are defined to be the average values of boundary points. Similarly, the values of ϕ *etc.* at the cell boundaries are defined as the average values of centering points.

4. Results and Discussion

4.1. Effects of dimensionless parameters. In this subsection, we're going to study effects of the dimensionless parameters on the dynamics of drop formation. We focus our attention on their effects on two dimensionless variables, limiting length L_D and volume of the drop V_D. Limiting length is defined to be the distance from the inner tube exit to the tip of the drop at the breakup. For each drop, V_D could be evaluated by $V_D = u_i\pi R_i^2 T_d$, where T_d is the time needed to form the drop. We measure L_D and V_D at "steady state", *i.e.*, when the limiting length and drop volume don't change with the drop number any more. For all cases, we keep

$S_l = 20$, $a = 3$, $nz = 200$, $nr = 30$, $\epsilon = 0.1$, $L_i = 2$, u_i=1.0, $Q_r = 10.0$, $U_o = \frac{Q_r}{a^2}$, $\mathcal{B} = \frac{3}{2\sqrt{2}\mathcal{C}a}$ and $s = 1.5$. For most of the simulations, $\triangle t = 2.67E - 3$, but it is adjusted to a smaller value for smaller $\mathcal{R}e$.

4.1.1. Effects of the Reynolds number $\mathcal{R}e$. Figure 2 shows the variation of (a) L_D and (b) V_D with $\mathcal{R}e$ at three different λ_η: $\lambda_\eta = 0.1$, $\lambda_\eta = 1$, and $\lambda_\eta = 10$. All the other dimensionless parameters are kept fixed at $Bo = 0.01$, $\mathcal{C}a = 0.01$, $\mathcal{L}_d = 0.05$, $\lambda_\rho = 0.1$. The inserts in figure 2 (a) represent drop shapes at the breakup for $\lambda_\eta = 0.1$, and that in figure 2 (b) represent the case for $\lambda_\eta = 10.0$. The corresponding values of $\mathcal{R}e$ for the inserts, from the left-most to the right-most, are 0.001, 1, 40 respectively in both (a) and (b).

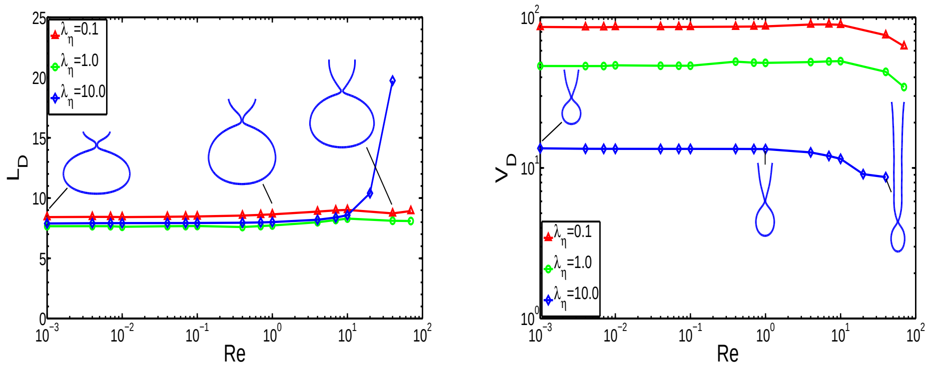

(a) (b)

FIGURE 2. Variation of (a) the limiting length L_D and (b) the primary drop volume V_D with the Reynolds number $\mathcal{R}e$ at three viscosity ratios, $\lambda_\eta = 0.1$, 1, and 10.0. Here, $Bo = 0.01$, $\mathcal{C}a = 0.01$, $\mathcal{L}_d = 0.05$, $\lambda_\rho = 0.1$.

Figure 2 shows that both L_D and V_D do not change much when $\mathcal{O}(10^{-3}) < \mathcal{R}e \leq 10$ for all the three cases we consider. When $\mathcal{R}e \geq 10$, V_D decreases for all cases, L_D increases significantly for $\lambda_\eta = 10.0$ while it increases slowly for the other two values of λ_η. As $\mathcal{R}e$ increases, the inertia of the drop increases. However, as long as the combination of the inertia force of drop itself and the viscous drag force from the outer fluid is not large enough to overcome the surface tension force, the fluid would break up near the orifice with very short limiting length. When λ_η increases, the viscous force from the outer fluid increases, making the volume of the drop become smaller. As λ_η increases to 10, the viscous drag force from the outer fluid is so large that it makes the drop move to a longer distance before the drop break up. The inserts show that for $\lambda_\eta = 0.1$ and $\mathcal{R}e$ small, there is a thin thread formed between the main drop and the liquid pendant to the tube. The reason, as explained by Suryo [25], is that more viscous inner fluid could not only dampen the oscillations of the drop interface, but also slow down the breakup process, leading to the formation of a thin thread. This thin thread becomes shorter and shorter as $\mathcal{R}e$ increases and it disappears completely when $\mathcal{R}e = 10$, at which the main drop connects to the pendant fluid directly. Figure 2 shows the same trends of variations of L_D and V_D with $\mathcal{R}e$ as figure 13.12 in Suryo's work [25] which is obtained by sharp interface method.

4.1.2. Effects of the Capillary number $\mathcal{C}a$. Capillary number measures the relative importance of the viscous force to surface tension force and plays an important role in the breakup behaviour of the drops. Figure 3 shows the variation of (a) L_D and (b) V_D with $\mathcal{C}a$ at three different λ_ρ: $\lambda_\rho = 0.1$, $\lambda_\rho = 1$, and $\lambda_\rho = 10$. All the other dimensionless parameters are kept fixed at $Bo = 0.01$, $\mathcal{R}e = 0.01$, $\lambda_\eta = 1.0$, $\mathcal{L}_d = 0.05$. The inserts to figure 3 (a) represent drop shapes at the breakup at four different $\mathcal{C}a$ for $\lambda_\rho = 10.0$ and the inserts to figure 3 (b) represent the case for $\lambda_\rho = 0.1$. The corresponding values of $\mathcal{C}a$ for the inserts, from the left-most to the right-most, are 0.004, 0.01, 0.04, and 0.07 respectively both in figure (a) and (b).

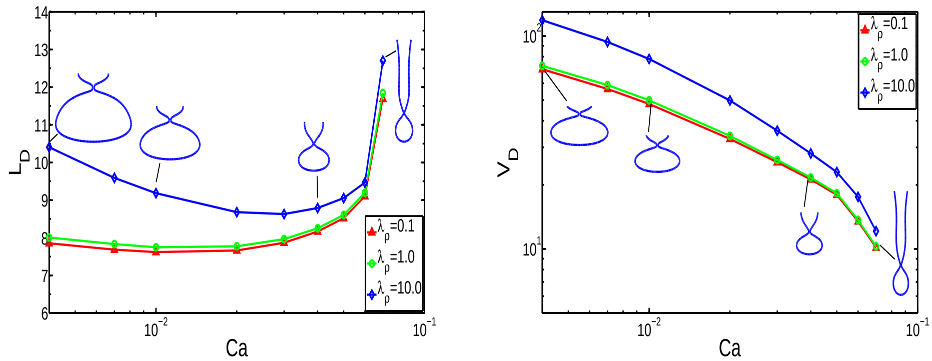

(a) (b)

FIGURE 3. Variation of (a) the limiting length L_D and (b) the primary drop volume V_D with the Capillary number $\mathcal{C}a$ at three density ratios, $\lambda_\rho = 0.1$, 1, and 10. Here, $Bo = 0.01$, $\mathcal{R}e = 0.01$, λ_η=1.0, $\mathcal{L}_d = 0.05$.

Figure 3 (a) shows that curves for $\lambda_\rho = 0.1$ and $\lambda_\rho = 1.0$ are nearly the same, while for $\lambda_\rho = 10.0$, the curve shows a bigger L_D than the other two curves. For all three curves, L_D first decreases as $\mathcal{C}a$ increases, but the rate of change of the curve at $\lambda_\rho = 10.0$ is larger than that at the other two values of λ_ρ. L_D then increases smoothly as $\mathcal{C}a$ continues to increase, and it suddenly increases to a much larger value when $\mathcal{C}a$ increases from 0.06 to 0.07 for all the three λ_ρ we consider, indicating a transition from dripping to jetting. Figure 3 (b) shows that V_D keeps decreasing as $\mathcal{C}a$ increases for all three cases. These phenomena can be explained as follows: when $\mathcal{C}a$ is small, surface tension force is large compared with the viscous force, so the drop is held back to the orifice. Longer time is needed for a drop to pinch off, and more fluid can flow into the drop, so the drop size is bigger. As $\mathcal{C}a$ increases, the viscous force plays more and more important role in drop formation, and the effect of surface tension becomes weaker, so the drop can move to longer distance before it breaks up. Force balance can be reached earlier, which helps to shorten drop formation period and form drops with smaller size. As the effects of viscous force large enough, the mechanics changes from dripping to jetting suddenly. Also, as the outer fluid overweight the inner fluid, fluid surrounding the drop also push it moving in the gravitational direction. The inserts in figure (a) and (b) tell us these variations in a more straightforward way. Furthermore, they show that the shape of the drop is not only affected by λ_ρ, but also by $\mathcal{C}a$. At $\lambda_\rho = 0.1$, the main drop is round, while at $\lambda_\rho = 10.0$, the main drop is more like a pear with lower half part bigger than the upper half part. For small $\mathcal{C}a$, there is a thin thread connecting the main drop to the pendant fluid, say, the first two drops in figure (a). As $\mathcal{C}a$ increases, the main drop becomes smaller while the pendant fluid becomes longer, at the same time, the thin thread disappears, so the main drop connects to the pendant jet directly. Our results shows the same trends as figure 13.13 in Suryo's work [25].

4.1.3. Effects of the viscosity ratio λ_η. Figure 4 shows the variation of (a) L_D and (b) V_D with λ_η at three $\mathcal{R}e$: $\mathcal{R}e = 1$, $\mathcal{R}e = 10$, and $\mathcal{R}e = 100$. All the other dimensionless parameters are kept fixed at $Bo = 0.01$, $\mathcal{C}a = 0.01$, $\mathcal{L}_d = 0.05$, $\lambda_\rho = 0.1$. The inserts to figure 4 (a) represent drop shapes at the breakup for $\mathcal{R}e = 100$, the corresponding values of λ_η, from the left-most to the right-most, are 0.001, 0.1, 1, 2 respectively, and the inserts to figure 4 (b) represent the case when $\mathcal{R}e = 1$, the corresponding λ_η, from the left-most to the right-most, is 0.001, 0.1, 10, and 20.

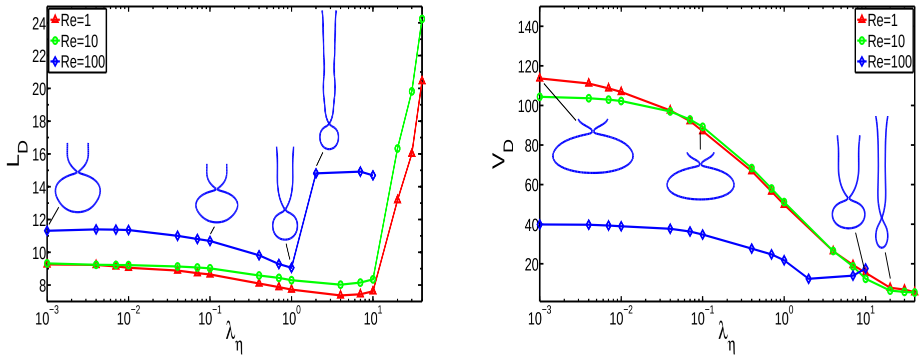

(a) (b)

FIGURE 4. Variation of (a) the limiting length L_D and (b) the primary drop volume V_D with the viscosity ratio λ_η at three Reynolds number, $\mathcal{R}e = 1$, 10, and 100. Here, $Bo = 0.01$, $\mathcal{C}a = 0.01$, $\mathcal{L}_d = 0.05$, $\lambda_\rho = 0.1$.

Figure 4 (a) shows that L_D keeps decreasing as λ_η increases from $\mathcal{O}(10^{-3})$ to $\mathcal{O}(1)$ for $\mathcal{R}e = 100$, or as λ_η increases from $\mathcal{O}(10^{-3})$ to $\mathcal{O}(10^1)$ for $\mathcal{R}e = 1$ or $\mathcal{R}e = 10$; L_D then increases suddenly to a large value for all three cases, indicating a transition from dripping to jetting. Figure 4 (b) shows that V_D keeps decreasing as λ_η increases. The curves for $\mathcal{R}e = 1$ and $\mathcal{R}e = 10$ are nearly the same when $\mathcal{O}(10^{-1}) \leq \lambda_\eta \leq 40$, but the curve for $\mathcal{R}e = 100$ is very different from the other two curves. At $\mathcal{R}e = 100$, V_D is much smaller than that of the other two Reynolds number. The inserts can also tell us these differences, furthermore, they show that at $\mathcal{R}e = 100$, the pendant drop forms a long jet connecting the main drop to the orifice, while at $\mathcal{R}e = 1$, the jet between the drop and the orifice is very short for small λ_η, but it increases as λ_η increases. When both $\mathcal{R}e$ and λ_η are small, the inertial force of the inner fluid as well as the viscous drag force of the outer fluid are relatively small, the surface tension force takes a major effect, so the drop breaks up in a position near the orifice. As λ_η increases, the viscous drag force from the outer fluid becomes bigger and bigger, the velocity in viscous force direction increases, which makes the drop moves longer downward and finally forms a long jet. When $\mathcal{R}e$ increases, the inertial force of the inner fluid which pushes the drop downward takes more and more effect, and the pendant fluid becomes longer and longer, forming a jet. Meanwhile, the increasing inertial force shortens drop formation time and decreases the drop size. The inserts also indicate that the drop shapes are affected by $\mathcal{R}e$. When $\mathcal{R}e = 100$, the lower half part of the drop is smaller than the upper half part, while the situation is different for $\mathcal{R}e = 1$. The trend of L_D with λ_η is similar to figure 13.15 (a) in Suryo's work [25] before $\mathcal{R}e = 10$. For $\mathcal{R}e > 10$, our results shows a different trend. The reason is that our result is obtained for drops at "steady state" when the system is in jetting regime, and their result is obtained for the first drop when the system has not developed to jetting regime. The trend of V_D is different from figure 13.15 (b) in Suryo's work [25] for $\mathcal{R}e = 100$, although for the other two values of $\mathcal{R}e$, they are similar.

4.1.4. Effects of the density ratio λ_ρ. Figure 5 shows the variation of (a) L_D and (b) V_D with λ_ρ at three λ_η: $\lambda_\eta = 0.1$, $\lambda_\eta = 1$, and $\lambda_\eta = 10$. All the other dimensionless parameters are kept fixed at $\mathcal{R}e = 0.1$, $Bo = 0.5$, $\mathcal{C}a = 0.01$, $\mathcal{L}_d = 0.05$. The inserts to figure 5 (a) represent drop shapes at the breakup when $\lambda_\eta = 10$, the corresponding values of λ_ρ, from the left-most to the right-most, are 0.01, 0.1, 1.0 respectively, and the inserts to figure 5 (b) represent the case when $\lambda_\rho = 0.1$, from the left-most to the right-most, $\lambda_\rho = 0.01, 0.1, 0.5, 1.0$.

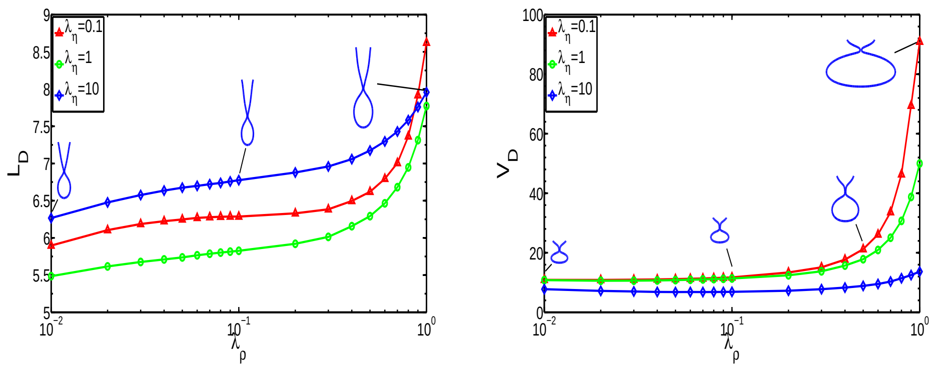

(a) (b)

FIGURE 5. Variation of (a) the limiting length L_D and (b) the primary drop volume V_D with the density ratio λ_ρ at three viscosity ratio, $\lambda_\eta = 0.1$, 1, and 10. Here, $\mathcal{R}e = 0.1$, $Bo = 0.5$, $\mathcal{C}a = 0.01$, $\mathcal{L}_d = 0.05$.

Figure 5 (a) shows that L_D keeps increasing as λ_ρ increases. When $\mathcal{O}(10^{-2}) < \lambda_\rho \leq 0.4$, the rate of change of L_D is small, but when $\lambda_\rho > 0.4$, the rate of change of L_D is relatively large, especially for $\lambda_\eta = 0.1$. Figure 5 (b) shows that V_D hardly changes as λ_ρ increases from $\mathcal{O}(10^{-2})$ to $\mathcal{O}(10^{-1})$. When $\lambda_\rho > \mathcal{O}(10^{-1})$, V_D starts to increase as λ_ρ increases, and it increases much quickly when $\lambda_\rho > 0.4$, especially for $\lambda_\eta = 0.1$. The inserts in figure 5 (a) and (b) gives a straightforward impression of those changes. V_D doesn't change a lot with λ_ρ at $\lambda_\eta = 10$, but at $\lambda_\eta = 0.1$, V_D is much larger at $\lambda_\rho = 1.0$ than that at $\lambda_\rho = 0.01$. We explain all those phenomena as follows: We first look at figure 5 (b), as λ_ρ increases and less than 1, the density difference between the inner fluid and the outer fluid decreases. This has the same effect as one reduces the gravitational force of a drop which pinches off in air. So surface tension force plays a major role in drop formation, longer time is needed for the drop to reach its force balance, more fluid can flow into the drop and result in an increase in V_D. Meanwhile, since the increase in λ_ρ doesn't affect the length of the pendant fluid very much, so the increase in V_D also leads to an increases in L_D. The inserts indicate that there is a thin thread connecting the main drop to the pendant liquid at $\lambda_\eta = 0.1$, however, at $\lambda_\eta = 10$, the main drop connects to the pendant liquid directly without a thin thread between them. The reason is that more viscous inner fluid can dampen or even eliminate the oscillation of the interface, which makes possible greater thread elongation and extension. Furthermore, the inserts in figure 5 (a) show a longer jet and a smaller drop than that in figure 5 (b). This is because a larger λ_η indicates a lager viscous drag force from the outer fluid, and it makes the drop move downward. So compared with drops in figure 5 (b), drops in figure 5 (a) have larger force in downward direction and shorter drop formation period. Figure 13.16 of Suryo's work [25] shows a different trend which indicates that λ_ρ doesn't affect L_D and V_D significantly while our results show they do. The reason is, their definition for $G \equiv \frac{(\rho_i-\rho_o)R_i^2 g}{\gamma}$ is different with our definition for $\mathcal{B}o \equiv \frac{\rho_c l_c^2 g}{\gamma} = \frac{\rho_i R_i^2 g}{\gamma}$. More specifically, we can related our $\mathcal{B}o$ with their G by the formula $G = -\mathcal{B}o(\lambda_\rho - 1)$, as λ_ρ changes, the relative gravitational force G will actually change. So we think it might be more reasonable to keep $\mathcal{B}o$ rather than G fixed.

4.1.5. Effects of the Bond number Bo**.** Figure 6 shows the variation of (a) L_D and (b) V_D with Bo at two different λ_η: $\lambda_\eta = 1.0$ and $\lambda_\eta = 10.0$. All the other dimensionless parameters are kept fixed at $\mathcal{R}e = 1.0$, $\mathcal{C}a = 0.01$, $\mathcal{L}_d = 0.05$, $\lambda_\rho = 0.1$. The inserts to figure 6 (a) represent drop shapes at the breakup for different Bond number at $\lambda_\eta = 1.0$ and inserts to figure 6 (b) represent the case at $\lambda_\eta = 10.0$. The values of Bo for the inserts, from the left-most to the right-most, are 0.0001, 0.01, 0.1 and 1 respectively in both figure (a) and (b). Figure 6 shows

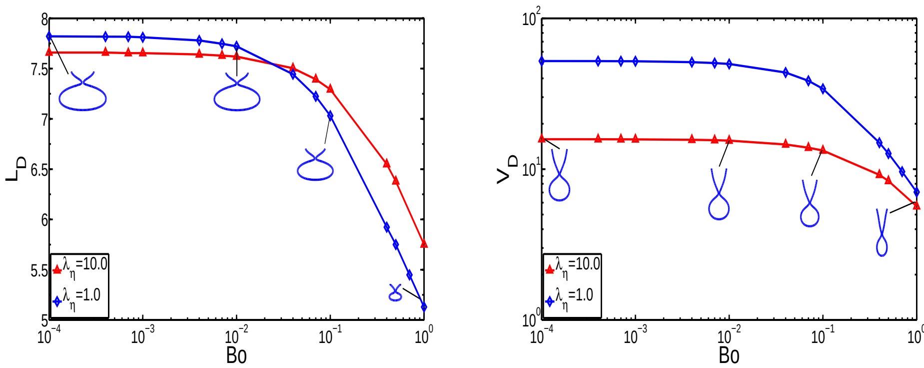

(a) (b)

FIGURE 6. Variation of (a) the limiting length L_D and (b) the primary drop volume V_D with the Bond Number Bo. Here, $\mathcal{R}e = 1.0$, $\mathcal{C}a = 0.01$, $\mathcal{L}_d = 0.05$, $\lambda_\rho = 0.1$.

that there is nearly no change in L_D as well as V_D when Bo increases from $\mathcal{O}(10^{-4})$ to $\mathcal{O}(10^{-2})$, this means that the effect of the gravitational force on drop formation can be ignored for those values of Bo; when $Bo > \mathcal{O}(10^{-2})$, the gravitational force starts to take effects and accelerate the drop breakup process. It takes shorter time for a drop to form and pinch off, thus smaller drops can be formed. We see from the inserts that the size of the drop decreases while the length of the pendant drop doesn't change very much, so both L_D and V_D decrease with the increasing Bo. The curve with $\lambda_\eta = 1.0$ decreases faster than the curve with $\lambda_\eta = 10.0$. The inserts show that one can also reduce the drop size by increasing λ_η. Because as λ_η increases, the outer fluid becomes more viscous and exerts larger force on the drop, dragging the drop moving downward. The variations of L_D and V_D show the same trends as figure 13.6 of Suryo's work [25].

4.1.6. Effects of the diffusion coefficient $\mathcal{L}_d$. Figure 7 shows the variation of (a) L_D and (b) V_D with $\mathcal{L}_d$ at three different λ_ρ, $\lambda_\rho = 0.1$, $\lambda_\rho = 1.0$ and $\lambda_\rho = 10.0$. All the other dimensionless parameters are kept fixed at $\mathcal{R}e = 1.0$, $\mathcal{C}a = 0.01$, $Bo = 0.01$, $\lambda_\eta = 10.0$. The inserts to figure 7 (a) represent drop shapes at the breakup for three different $\mathcal{L}_d$ at $\lambda_\rho = 10.0$ and the inserts to figure 7 (b) represent the case at $\lambda_\rho = 1.0$. The values of $\mathcal{L}_d$ for the inserts, from the left-most to the right-most, are 0.01, 0.1 and 0.7 respectively both in figure (a) and (b).

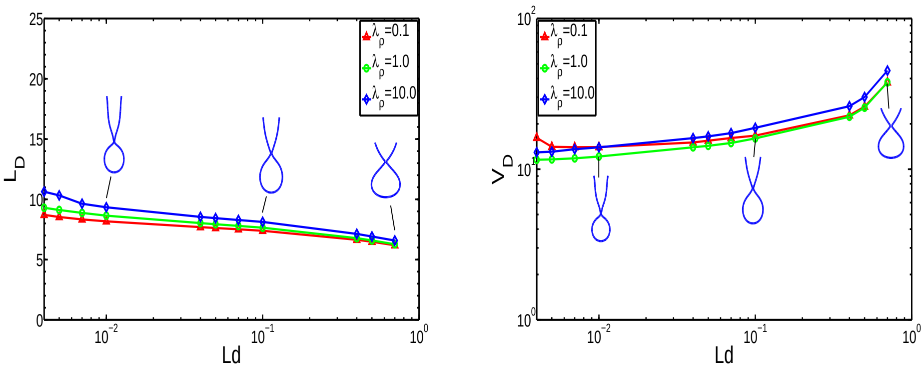

(a) (b)

FIGURE 7. Variation of (a) the limiting length L_D and (b) the primary drop volume V_D with the parameter $\mathcal{L}_d$. Here, $\mathcal{R}e = 1.0$, $\mathcal{C}a = 0.01$, $Bo = 0.01$, $\lambda_\eta = 10.0$.

Figure 7 shows that the variations of L_D and V_D with $\mathcal{L}_d$ are nearly the same for all the three λ_ρ we consider. L_D decreases slowly as $\mathcal{L}_d$ increases, and V_D increases slowly as $\mathcal{L}_d$ increases. The parameter $\mathcal{L}_d$ is mobility constant. The phase field model is expected to converge to the sharp interface model when both $\mathcal{L}_d$ and ϵ become small. These two parameters are numerical constants to smooth out the jump discontinuity across the interface. They should be kept small so that they do not affect the physical properties of the system. Figure 7 does show that V_D and L_D do not change much for small $\mathcal{L}_d$.

4.2. Comparison with the experiments. In this subsection, we compare our numerical results with two experiments done by Zhang [34] and Utada et al. [29].

4.2.1. Comparison with the experimental results by Zhang [34]**.** Based on CSF + VOF method, Zhang [34] investigated bubble formation dynamics when a viscous liquid is injected through a vertical tube into another immiscible and viscous fluid. They focused on the dripping region where the dispersed fluid flowed through the capillary tube at small flow rate. Good agreement was found between the numerical results and their experimental results. We now compare our numerical results with their experiment. The 2-ethyl-1-hexanol is the dispersed fluid and distilled water is the outer fluid. The viscosities of the inner and outer fluids are 0.089 $g\ cm^{-1}\ s^{-1}$ and 0.01 $g\ cm^{-1}\ s^{-1}$, the densities of the inner and outer fluids are 0.83 $g\ cm^{-3}$ and 1.0 $g\ cm^{-3}$, respectively. Interfacial tension is 13.2 $g\ s^{-2}$. The dispersed fluid flows through a tube of radius 0.16 cm at the flow rate $Q = 5\ ml/min = \frac{1}{12}\ cm^3/s$, and the outer fluid is quiescent. With these data, we can calculate the dimensionless parameters: $\mathcal{R}e = \frac{\rho_i Q_i}{\eta_i \pi R_i} = 1.5461$, $\mathcal{C}a = \frac{\eta_i Q_i}{\gamma \pi R_i^2} = 0.006986$, $Bo = \frac{\rho_i R_i^2 g}{\gamma} = 1.5776$, $\mathcal{B} = \frac{3}{2\sqrt{2}\mathcal{C}a}$, $\lambda_\rho = \frac{\rho_o}{\rho_i} = 1.2048$, $\lambda_\eta = \frac{\eta_o}{\eta_i} = 0.1123$. We then simulate the dimensionless system with the following settings: $S_l = 20$, $a = 4$, $nz = 200$, $nr = 40$, $\epsilon = 0.1$, $L_i = 2$, $u_i = 1.0$, $Q_r = 0$, $s = 1.5$, $\mathcal{L}_d = 0.156$.

Figure 8 compares the time sequence of bubble shapes of our numerical results with Zhang's experiment. From 1 to 9, the time sequences for the left half parts (experiment) are $t = 0.6s$, $0.91s$, $1.21s$, $1.25s$, $1.27s$, 1.2712, $1.272s$, $1.275s$, $1.276s$, and for the right half parts (numerical results) are $t = 0.6019s$, $0.9070s$, $1.2121s$, $1.2533s$, $1.2699s$, $1.2712s$, $1.2719s$, $1.2752s$, $1.2760s$. It shows that our numerical results matches well with Zhang's experiment.

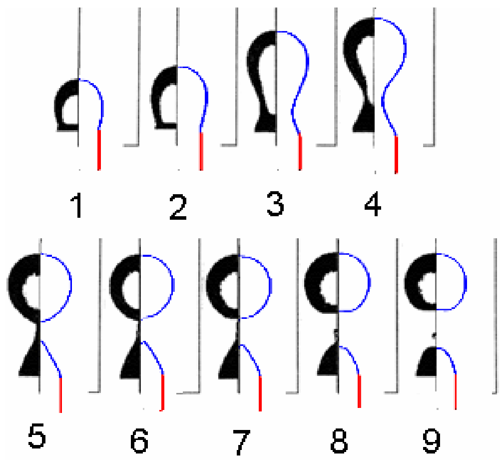

FIGURE 8. Comparison of the time sequences of bubble shapes. Right half parts are our numerical results, left half parts are reprinted from *Chem. Eng. Sci.*, X. Zhang, Dynamics of drop formation in viscous flows, **54**, 1759-1774 (1996), Copyright Elsevier (1996).

4.2.2. Comparison with the experimental results by Utada et al. (2007). The dynamics of drop formation can be classified into two regimes. One is dripping where drops are formed near the tube exit, and the other is jetting where drops break up away from the orifice and connect to the tube exit through a long and thin jet. Dripping occurs at low flow rates while jetting occurs at high flow rates. Using deionized water and polydimethylsiloxane (PDMS) oils with different viscosities, Utata et al. [29] tested two classes of dripping to jetting transition. The first class is controlled by the critical Capillary number of the outer fluid $\mathcal{C}_o = \frac{\eta_o u_o}{\gamma}$, which measures the balance between the viscous shear stress on the drop and the surface tension force. When $\mathcal{C} > \mathcal{C}_o$, a jet forms which thins as it moves downstream. The second class is controlled by the critical weber number of the inner fluid $\mathcal{W}_i = \frac{\rho_i d_{tip} u_i^2}{\gamma}$, which measures the balance between the inertial force of the inner fluid and the surface tension force, d_{tip} represents the diameter of the inner tube. This class of transition is different from the first one. Instead of decreasing, the jet diameter increases along its length. Utada et al. [29] tested the critical weber number $\mathcal{W}_i$ and the critical Capillary number $\mathcal{C}_o$ for different cases and showed that dripping to jetting transition occurred when $\mathcal{C}_o + \mathcal{W}_i \approx \mathcal{O}(1)$.

We now compare our numerical results with their experiments. Table 1 lists the densities, viscosities of the inner and outer fluids, and surface tension between the two fluids for different cases. When $\eta_i/\eta_o < 1$, the continuous phase is PDMS and the dispersed phase is water; when $\eta_i/\eta_o \geq 1$, the continuous phase is water and the dispersed phase is PDMS. The diameters of the inner and outer tubes in Utada's experiments are $R_i = 10\ \mu m$ and $R_o = 15\ \mu m$. In our simulation, we use a bigger $R_o = 30\ \mu m$. Given the dimensionless parameter $\mathcal{W}_i = \frac{2R_i\rho_i\tilde{u}_i^2}{\gamma}$ and $\mathcal{C}_o = \frac{\eta_o\tilde{U}_o}{\gamma}$, we can calculate the dimensional average velocities for the inner and outer fluids: $\tilde{u}_i = \sqrt{\frac{\gamma\mathcal{W}_i}{2\rho_i R_i}}$, $\tilde{U}_o = \frac{\gamma\mathcal{C}_o}{\eta_o}$. Then, the dimensionless parameters used in the system of equations can be obtained by: $\mathcal{R}e = \frac{\rho_i\tilde{u}_i R_i}{\eta_i}$, $\mathcal{C}a = \frac{\eta_i\tilde{u}_i}{\gamma}$, $Bo = \frac{\rho_i R_i^2 g}{\gamma}$, $Q_i = \tilde{u}_i R_i^2\pi$, $Q_o = \tilde{U}_o R_o^2\pi$, $Q_r = \frac{Q_o}{Q_i}$, $u_i = 1.0$, $U_o = \frac{\tilde{U}_o}{\tilde{u}_i} = \frac{Q_r}{a^2}$. Other settings used in the simulation are: $S_l = 40$, $a = 3$, $nz = 400$, $nr = 30$, $\epsilon = 0.1$, $L_i = 2$, $s = 1.5$, $\mathcal{L}_d = 0.25$, $\triangle t = 2.67E-3$. As a typical example, we first show in figure 9 and

Table 1. physical parameters for each symbol (P: PDMS, w: water).

symbol	γ	ρ_i	ρ_o	η_i	η_o
	$[g/s^2]$	$[g \cdot cm^{-3}]$	$[g \cdot cm^{-3}]$	$[g \cdot cm^{-1} \cdot s^{-1}]$	$[g \cdot cm^{-1} \cdot s^{-1}]$
triangle	40	0.97(P)	1.0(w)	0.1	0.01
star	4	0.97(P)	1.0(w)	0.1	0.01
diamond	40	0.97(P)	1.0(w)	0.01	0.01
hexagon	40	1.0(w)	0.97(P)	0.01	0.1
square	40	1.0(w)	0.97(P)	0.01	1.0

figure 10 two classes of transition observed in our numerical simulation for the case represented by the symbol "star". The transition in figure 9 is caused by increasing the Capillary number of the outer fluid $\mathcal{C}_o$. The jet thins as it moves downward. The transition in figure 10 is caused by increasing the weber number of the inner fluid $\mathcal{W}_i$. Instead of thinning, the jet becomes wider.

Figure 11 compares the state diagram of our numerical results with figure 4 in the paper of Utada et al. [29]. Dripping to jetting transition is plotted as a function of $\mathcal{C}_o$ and $\mathcal{W}_i$. Filled symbols represent dripping and hollow symbols represent jetting. Symbols "square", "hexagon", "triangle", "star" in both figure 11 (a) and (b) represent the same cases, the case represented by the symbol "diamond" in figure 11 (a) is the same as that represented by the symbol "pentagon" in figure 11 (b); the symbol "diamond" in figure 11 (b) represents the case where $\frac{\eta_i}{\eta_o} = 0.01$

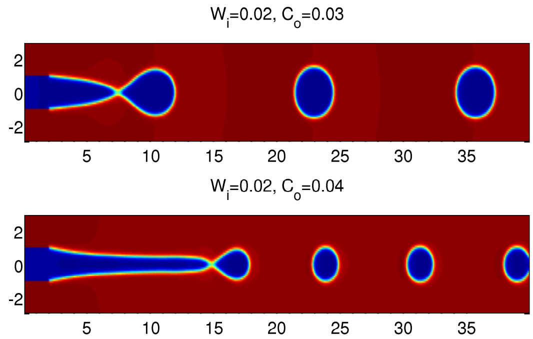

FIGURE 9. Dripping to jetting transition for "star" when keeping $\mathcal{W}_i = 0.06$ fixed, increasing $\mathcal{C}_o$ from 0.03 to 0.04.

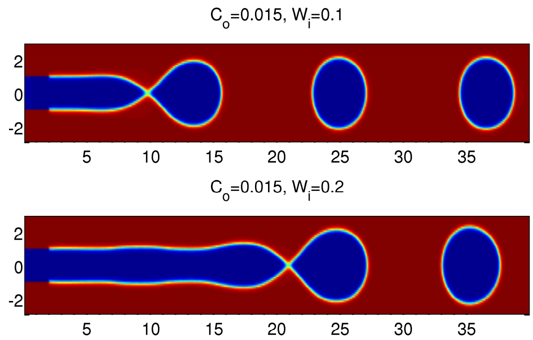

FIGURE 10. Dripping to jetting transition for "star" when keeping $\mathcal{C}_o = 0.015$ fixed, increasing $\mathcal{W}_i$ from 0.1 to 0.2.

with the extra capillary tube to increase U_o, and $\gamma = 40mN/m$; and the symbol "circle" in figure 11 (b) represents the case where $\frac{\eta_i}{\eta_o} = 0.1$ with the extra capillary tube to increase U_o, and $\gamma = 40mN/m$. Figure 11 shows that our results are in qualitative agreement with the experimental results.

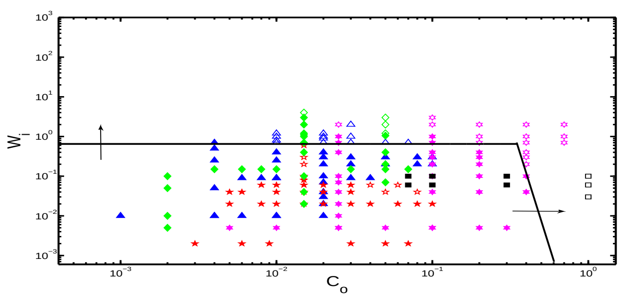

FIGURE 11. State diagrams of the dripping to jetting transition in a coflowing stream as a function of $\mathcal{C}_o$ and $\mathcal{W}_i$.

5. Conclusion

Based on phase field model, we study dynamics of drop formation when a fluid is injected into another immiscible, coflowing fluid. The effect of various physical parameters on the drop dynamics are studied systematically and the results are also compared with the previous work [25]. Furthermore, we compare the numerical results with Zhang's experiment [34]. The shape of the bubble during its evolution matches well with the experiment. Finally, we compare our numerical results with the experimental results of Utada et al. [29] on the dripping to jetting transition. Qualitative agreement with their experiment is found. The simulation results demonstrate that the process of drop formation can be reasonably predicated by the phase field model we used.

Acknowledgement

We are grateful to Dr. Min Gao, who shares with us his code for two phase moving contact problem with equal density and viscosity, and contributes many insightful discussions. We also thank Dr. Siu Long Lei for sharing his code for drop formation in two-phase flows with equal density and viscosity, and for his patience in answering many questions related to his paper [18]. Our thanks also go to Dr. Andrew S. Utada, who gives us his experiment data and answers many questions related to the paper [29].

References

[1] D. M. Anderson, G. B. McFadden and A. A. Wheeler, Diffuse-interface methods in fluid mechanics, Ann. Rev. Fluid Mech., 30 (1998) 139-165.

[2] J. U. Brackbill, D. B. Kothe and C. Zemach, A continuum method for modeling surface tension, J. Comp. Phys., 100 (1992) 335-354.

[3] R. B. Bird, W. E. Stewart and E. N. Lightfoot, Transport Phenomena, 2nd ed., Wiley, New York, 2002.

[4] A. J. Chorin, Numerical solution of the Navier-Stokes equations, Math. Comput., 22 (1968) 745-762.

[5] A. Carlson, M. Do-Quang and G. Amberg, Droplet dynamics in a bifurcating channel, Int. J. Multiphase Flow, 36 (2010) 397-405.

[6] C. Cramer, P. Fischer and E. J. Windhab, Drop formation in a co-flowing ambient fluid, Chem. Eng. Sci., 59 (2004) 3045-3058.

[7] S. C. Chuang and V. W. Goldschmidt, Bubble formation due to a submerged capillary tube in quiescent and coflowing streams, Trans. ASMED: J. Basic Eng., 92 (1970) 705-711.

[8] D. J. Eyre, *Unconditionally gradient stable time marching the Cahn-Hilliard equation*, In: J. Bullard, R. Kalia, M. Stoneham and L.-Q. Chen, Editors, Computational and Mathematical Models of Microstructural Evolution, The Materials Research Society, 1998.

[9] A. M. Gañán-Calvo, Generation of steady liquid micro-threads and micron-sized monodisperse sprays in gas streams, Phys. Rev. Lett., 80 (1998) 285-288.

[10] A. M. Gañán-Calvo and J. M. Gordillo, Perfectly monodisperse microbubbling by capillary flow focusing, Phys. Rev. Lett., 87 (2001) 274501.

[11] P. Garstecki, M. J. Fuerstman and G. M. Whitesides, Nonlinear dynamics of a flow-focusing bubble generator: An inverted dripping faucet, Phys. Rev. Lett., 94 (2005) 234502.

[12] J. L. Guermond, P. Minev and J. Shen, An overview of projection methods for incompressible flows, Comput. Methods Appl. Mech. Eng., 195 (2006) 6011-6045.

[13] J. L. Guermond and A. Salgado, A splitting method for incompressible flows with variable density based on a pressure Poisson equation, J. Comput. Phys., 228 (2009) 2834-2846.

[14] M. Gao and X. P. Wang , A Gradient Stable Scheme for a Phase Field Model for the Moving Contact Line Problem, J. Comput. Phys., (2011) doi: 10.1016/j.jcp.2011.10.015.

[15] C. W. Hirt and B. D. Nichols, Volume of fluid VOF method for the dynamics of free boundaries, J. Comput. Phys., 39 (1981) 201-225.

[16] J. Hua, B. Zhang and J. Lou, Numerical simulation of microdroplet formation in coflowing immiscible liquids, AIChE J., 53 (2007) 2534-2548.

[17] D. Jacqmin, Calculation of two-phase Navier-Stokes flows using phase-field modeling, J. Comp. Phys., 155 (1999) 96-127.

[18] S.L. Lei, Phase-field simulations of two-phase flows, Ph.D. thesis, The Hong Kong University of Science and Technology, Hong Kong, 2009.

[19] H. N. Oğuz and A. Prosperetti, Dynamics of bubble growth and detachment from a needle, J. Fluid Mech., 257 (1993) 111-145.

[20] T. Z. Qian, X. P. Wang and P. Sheng, Molecular scale contact line hydrodynamics of immiscible flows, Phys. Rev. E, 68 (2003) 016306.

[21] T.Z. Qian, X. P. Wang and P. Sheng, A variational approach to moving contact line hydrodynamics, J. Fluid Mech., 564 (2006) 333-360.

[22] J. R. Richards, A. N. Beris and A. M. Lenhoff, Steady laminar-flow of liquid-liquid jets at high Reynolds-number, Phys. Fluids, 5 (1993) 1703-1717.

[23] J. R. Richards, A. M. Lenhoff and A. N. Beris, Dynamics breakup of liquid-liquid jets, Phys. Fluids, 6 (1994) 2640-2655.

[24] J. R. Richards, A. N. Beris and A. M. Lenhoff, Drop formation in liquid-liquid systems before and after jetting, Phys. Fluids, 7 (1995) 2617-2630.

[25] R. Suryo, Breakup of simple and compound drops and bubbles, Ph.D. thesis, Purdue University, West Lafayette, Indiana, 2006.

[26] J. Shen, Modeling and numerical approximation of two-phase incompressible flows by a phase field approach, Lecture Note Series, IMS, National University of Singapore, 2011.

[27] R. Suryo and O. A. Basaran, Tip streaming from a liquid drop forming from a tube in a co-flowing outer fluid, Phys Fluids, 18 (2006) 082102.

[28] J. Shen and X. F. Yang, A Phase-Field Model and Its Numerical Approximation for Two-Phase Incompressible Flows with Different Densities and Viscosities, SIAM J. Sci. Comput., 32 (2010) 1159-1179.

[29] A. S. Utada, A. Fernandez-Nieves, H. A. Stone and D. A. Weitz, Dripping to Jetting Transitions in Coflowing Liquid Streams, Phys. Rev. Lett., 99 (2007) 094502.

[30] A. S. Utada, E. Lorenceau, D. R. Link, P. D. Kaplan, H. A. Stone and D. A. Weitz, Monodisperse double emulsions generated from a microcapillary device, Science, 308 (2005) 537-541.

[31] P. B. Umbanhowar, V. Prasad and D. A. Weitz, Monodisperse emulsion generation via drop breakup off in a coflowing stream, Langmuir, 16 (2000) 347-351.

[32] H. Wong, D. Rumschitzki and C. Maldarelli, Theory and experiment on the low Reynolds number expansion, contraction and detachment of a bubble pinned at the tip of a submerged capillary, J. Fluid Mech., 356 (1998) 93-124.

[33] X. Yang, J. J. Feng, C. Liu and J. Shen, Numerical simulations of jet pinching-off and drop formation using an energetic variational phase-field method, J. Comput. Phys., 218 (2006) 417-428.

[34] X. Zhang, Dynamics of drop formation in viscous flows, Chem. Eng. Sci., 54 (1999) 1759-1774.

[35] C. Zhou, P. Yue and J. J. Feng, Formation of simple and compound drops in microfluidic devices, Phys. Fluids, 18 (2006) 092105.

[36] D. F. Zhang and H. A. Stone, Drop formation in viscous flows at a vertical capillary tube, Phys. Fluids, 9 (1997) 2234.

[37] M. Gao and X. P. Wang, An efficient scheme for a phase field model for the moving contact line problem with variable density and viscosity, J. Comput. Phys., 272 (2014) 704-718.

Department of Mathematics, The Hong Kong University of Science and Technology, Hong Kong

E-mail: `jieweihk@gmail.com` and `mawang@ust.hk`